

The Contribution of Stars, Dust, Neutral Gas and SMBHs in Galaxies to the Cosmic Baryon Inventory

Jordan C. J. D’Silva,¹★ Simon P. Driver,¹ Aaron S. G. Robotham¹ Andrew Battisti,^{1,2} Elisabete da Cunha,¹ Luke J. M. Davies,¹ Stephen Eales,³ Claudia del P. Lagos¹

¹ International Centre for Radio Astronomy Research (ICRAR), University of Western Australia, Crawley, WA 6009, Australia

² Research School of Astronomy and Astrophysics, Australian National University, Cotter Road, Weston Creek, ACT 2611, Australia

³ Cardiff Hub for Astrophysics Research and Technology, Cardiff University, The Parade, Cardiff CF24 3AA, UK

arXiv:2601.08112v1 [astro-ph.GA] 13 Jan 2026

Accepted XXX. Received YYY; in original form ZZZ

ABSTRACT

We compute the cosmic stellar, dust and neutral gas mass history at $0 < z \lesssim 3$ using PROSPECT spectral energy distribution modelling of $\approx 800\,000$ galaxies in the Galaxy and Mass Assembly (GAMA) survey and the Deep Extragalactic VIIsible Legacy Survey (DEVILS). The cosmic dust mass history broadly follows the shape of the cosmic star formation history; though, the decline is slower, suggestive of a slowing rate of dust growth and destruction as the star formation declines past its peak at $z \approx 2$. Neutral gas masses were estimated by scaling the dust masses by the metallicity-dependent dust-to-gas ratio. The neutral gas mass density as traced by the dust is an average of ≈ 0.6 dex lower than that measured from 21cm experiments, most likely due to differences in the spatial scales inhabited by dust and HI. Folding in measurements of the supermassive black hole mass density obtained previously with similar data and methods, we present a self-consistent census of the baryons confined to galaxies. Stars, neutral gas, SMBHs and dust contained within the optical radii of galaxies account for ≈ 5 per cent of the baryons. Most of the remaining ≈ 95 per cent of baryons must be ionised and dispersed throughout the interstellar, circumgalactic and intergalactic media within, around and between galaxies.

Key words: keyword1 – keyword2 – keyword3

1 INTRODUCTION

Only ≈ 4 per cent of the contents of the Universe are in the form of baryons (Aghanim et al. 2020). It is thought that the bulk of those baryons are ionised and in the intergalactic medium, with the neutral fraction only about 1 part in 10^5 at $z \approx 5$ (Bosman et al. 2022) following cosmic reionisation. The fraction of baryons inside of the galaxies is $\lesssim 10$ per cent (de Graaff et al. 2019). The stars and active galactic nuclei (AGNs) in galaxies are responsible for the second largest repository of extragalactic photons incident on the Earth after the cosmic microwave background radiation, radiating especially in the radio, optical and infrared wavelengths (Driver et al. 2016; Koushan et al. 2021; Tompkins et al. 2023; Chiang et al. 2025). So, quantifying the baryon budget in galaxies is of great interest, particularly in connection to the astrophysical processes of star formation, chemical enrichment and the growth of supermassive black holes (SMBHs).

Since $z \approx 2$, the cosmic star formation history has declined by a factor of ≈ 10 on account of the depletion and consumption of their gas reservoirs (Madau & Dickinson 2014; Péroux & Howk 2020). The cosmic stellar mass history (CSMH) continues to steadily increase as the stellar mass cumulatively adds up with star formation (Wright et al. 2018; Driver et al. 2018; Thorne et al. 2021; Shuntov et al. 2025). A product of stellar mass assembly is chemical en-

richment and the formation of dust grains. Asymptotic giant branch stars produce dust grains in their circumstellar envelopes that can be released into the interstellar medium (ISM) via stellar winds (e.g., Ventura et al. 2014; Höfner & Olofsson 2018; Höfner & Freytag 2020). Dust also enters the ISM through supernovae explosions (e.g., Nomoto et al. 2006; Sarangi et al. 2018; Marassi et al. 2019; Bocchio et al. 2016; Schneider & Maiolino 2024), and can continue to condense in the remnants (Wooden et al. 1993; Matsuura et al. 2011). Dust growth may be tempered when, for example, the grains are destroyed in the tumultuous ISM or through astration where the dust is entombed in newly formed stars (Draine & Salpeter 1979a,b; Jones et al. 1994, 1996; Micelotta et al. 2018; Dayal et al. 2022).

Dust is a critical component of galaxies especially due to its effect on their light distributions. Photons with wavelengths largely between the far ultraviolet (FUV) to optical from stars and AGNs are attenuated and the absorbed energy is reradiated in the infrared (IR), mid infrared (MIR) and far infrared (FIR) (e.g., Trumpler 1930; Draine 2003). The energy balance argument means that the reradiated emission is a tracer of star formation as the young stars heat up the dust (Kennicutt Jr & Evans II 2012; Davies et al. 2016). The cosmic dust mass history (CDMH) encodes the balance between dust growth and destruction that, consequently, contains clues for recipes of chemical enrichment and feedback in galaxy formation models (Somerville & Davé 2015; Trayford et al. 2025).

Dust grains are known to be catalysts for molecular hydrogen formation as H₂ molecules condense on their surfaces. (Wakelam

★ E-mail: jordan.dsilva@research.uwa.edu.au

et al. 2017). This is particularly useful because H_2 is notoriously hard to observe in the normal conditions of the giant molecular clouds where the temperatures are generally too low to excite the molecules. In lieu of viable direct H_2 measurements, tracers are observed instead, such as CO, CI and [CII] (Zanella et al. 2018; Madden et al. 2020; Dunne et al. 2022). Dust is also a tracer of H_2 to complement the tracers based on carbon (Dunne et al. 2022).

In this paper, we conduct a census of the baryons confined to galaxies, taking into account the contribution from, in particular, the dust and the neutral gas traced by dust. We do this with spectral energy distribution (SED) fitting, building on from a similar census of stars and dust undertaken by Driver et al. (2018) who used SED fitting on $\sim 10^5$ galaxies.

The novelty of this work is to compute the redshift evolution of the dust and neutral gas content, and its connection to most of the remaining baryons in galaxies, in a self-consistent way. Specifically, we will use the homogeneous data and SED fitting results at $0 < z < 3$ from the Galaxy And Mass Assembly (GAMA, Driver et al. 2011, 2022) survey and the Deep Extragalactic VIsible Legacy Survey (DEVILS, Davies et al. 2018; Davies et al. 2025). A critical advantage of this data set is that the evolution of cosmic dust and neutral gas is then easily and directly comparable to the volume-averaged evolution of stellar mass, star formation rate and SMBH growth also inferred with GAMA and DEVILS. Weighing the baryons in this manner means that the mass budget in galaxies can be easily combined with the equivalent mass budget in the cosmic web to account for most, if not all, of the visible matter in the entire Universe (e.g., Macquart et al. 2020; Connor et al. 2025).

The outline of the paper is as follows. The data is described in Section 2. The main results are presented in Section 4, 5 and 6. Our final conclusions and summary of the work is in Section 7. We use Planck ΛCDM cosmology with $H_0 = 68.4 \text{ km s}^{-1} \text{ Mpc}^{-1}$, $\Omega_\Lambda = 0.699$ and $\Omega_M = 0.301$ (Aghanim et al. 2020).

2 DATA

2.1 Photometry

GAMA and DEVILS are vast volume-complete, spectro-photometric surveys, covering $0 < z < 4$ with high completeness. Both surveys are complemented by FUV-FIR photometric measurements as processed by the source finding software, PROFOUND (Robotham et al. 2018). The details of the photometric extraction can be found in Bellstedt et al. (2020a) for GAMA and Davies et al. (2021) for DEVILS. For both GAMA and DEVILS the source detection was first performed on the $r + Z$ (GAMA) and $Y + J + H$ (DEVILS) bands to extract UV-optical-NIR photometry. MIR-FIR photometry for both surveys was extracted using a point-spread-function (PSF) aperture approach to account for the differences in both the spatial resolution and sensitivity of the different images. The source positions for the PSF photometry were obtained from the optically selected catalogue.

For DEVILS, PSF photometry was not sought for every source in the $Y + J + H$ selected catalogue because the Y -flux is not well correlated with the expected emission at longer wavelengths and the lower resolution of the MIR-FIR data meant that some sources will be confused with multiple input galaxies occupying the same resolution element (Davies et al. 2021). PSF fitting was first performed on the $24\mu\text{m}$ Multiband Imaging Photometer for Spitzer (MIPS24) imaging (Sanders et al. 2007) using the coordinates of a sample of $Y < 21.2$ mag objects. The PSF fitting routine also extracted sources that were bright in the MIPS24 imaging but had no clear

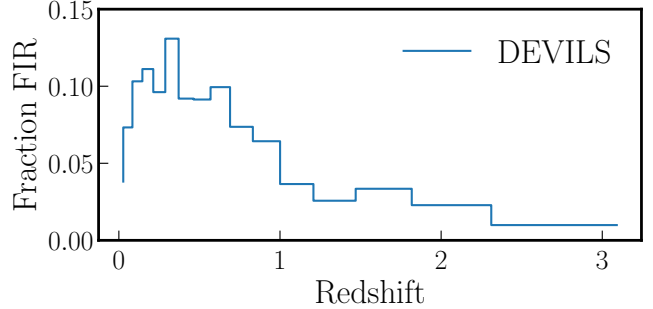


Figure 1. Fraction of sources with FIR photometric observations in the DEVILS sample.

UV-MIR counterpart in the initial $Y < 21.2$ mag sample. For these sources, a likely counterpart was assigned by cross matching the source coordinates against the positions in the full UV-MIR catalogue (including $Y > 21.2$ mag objects). The $Y - 24\mu\text{m}$ colour was also cross matched against $Y - 24\mu\text{m} \approx 3$ mag, which was identified as the typical colour for the of the $Y < 21.2$ mag sample. This process of matching will fail for sources with atypical $Y - 24\mu\text{m}$ colours, such as AGN, but likely these only constitute a small fraction of the entire sample. The source positions from the MIPS24 sample were then used for further PSF photometry in the MIPS70 band and the *Herchel* $P100, P160, S250, S350, S500$ bands (Lutz et al. 2011; Oliver et al. 2012). Figure 1 shows that the fraction of MIR-FIR observations in the DEVILS sample is ≈ 10 per cent at $z \approx 0.3$ and decreases to ≈ 1 percent at $z > 2$.

No attempt was made to measure the FIR photometry for objects that did not satisfy the above requirements (i.e., $Y > 21.2$ mag sources without any MIPS24 counterpart), and the fluxes have no value. A small fraction of FIR objects were detected with no clear counterpart in either the optical or MIPS24 bands. These objects were not included in the DEVILS SED fitting results because they were not associated with a DEVILS target.

A similar PSF extraction was performed on the GAMA imaging but, unlike DEVILS, the imaging was wider and shallower meaning that FIR photometry could be extracted for essentially all optically detected sources (Thorne et al. 2021). We only use the D10 sub-survey of DEVILS in the COSMOS field because of its spectroscopic and photometric redshift completeness that is complemented by previous surveys (e.g., zCOSMOS, Lilly et al. 2009) and to aid in comparison with previous works (Thorne et al. 2021; D'Silva et al. 2023).

2.2 SED fits

The SEDs were fit using PROSPECT (Robotham et al. 2020), in work first presented in Bellstedt et al. (2020b) for GAMA and Thorne et al. (2021, 2022a) in the D10-COSMOS field of DEVILS. These previous SED fits of $\approx 800\,000$ galaxies between GAMA and DEVILS-D10 are used in this work. PROSPECT models the FUV-FIR emission of galaxies under the assumption of energy balance.

The intrinsic stellar emission is modelled with the Bruzual & Charlot (2003) stellar population synthesis library, the Chabrier (2003) IMF and a flexible skewed-normal, parametric star formation history.

The intrinsic star light is then attenuated using the Charlot & Fall (2000) model. Attenuation as a function of wavelength is calculated as

$$A(\lambda) = e^{-\tau_V(\lambda/\lambda_0)^{-0.7}}, \quad (1)$$

where $\lambda_0 = 5500 \text{ \AA}$ and τ_V is the V -band normalising coefficient of the optical depth. This is a two component model where light is attenuated both by stellar birth clouds and the ISM, however only stars younger than 10 Myr will have their light affected by the birth clouds. Hence, in ProSPECT the two parameters that control the attenuation are τ_V^{BC} and τ_V^{ISM} .

The metallicity is implemented as an evolutionary model that scales linearly with the stellar mass growth and chemical enrichment. The initial metallicity is assumed to be $Z = 10^{-4}$ that is the lowest metallicity template in the [Bruzual & Charlot \(2003\)](#) stellar population synthesis library. The parameter to be fitted is the final metallicity at the epoch of observation (Z_{final}) that represents the metallicity of the gas from which the final generation of stars formed. Z_{final} for a fitted galaxy is closest to the gas-phase metallicity measured from spectral lines, unless the gas content of the galaxy changed significantly after the last epoch of star formation. For example, if the galaxy continued to accrete metal-poor gas then Z_{final} would be higher than the gas-phase metallicity ([Thorne et al. 2022b](#)).

The attenuated light is then assumed to be reradiated in the IR-FIR as per the [Dale et al. \(2014\)](#) dust emission models. These models were computed by combining the emission curves of large dust grains with particle sizes $\sim 100 \text{ nm}$, small grains with sizes $\sim 10 \text{ nm}$ and polycyclic aromatic hydrocarbon (PAH) molecules with sizes $\sim 1 \text{ nm}$ ([Desert et al. 1990](#)) after exposing them to a variety of radiation fields with various levels of intensity, U ([Dale et al. 2001; Dale & Helou 2002](#)). The [Dale et al. \(2014\)](#) models envisage the total dust emission of a galaxy as an ensemble of local dust emission SEDs exposed to radiation fields with a range of intensities, $0.3 \leq U \leq 10^5$, where $U = 1$ is the intensity in the solar neighbourhood.

In the [Dale et al. \(2014\)](#) models, the distribution of the strengths of the local radiation fields is controlled by the parameter α , such that

$$dM_{\text{dust}} \propto U^{-\alpha} dU, \quad (2)$$

where dM_{dust} are the local dust masses exposed to the radiation fields. Small values of α produce lower dust masses than larger values because hot, large dust grains dominate the emission ([Dale & Helou 2002](#)). PROSPECT considers a superposition of two [Dale et al. \(2014\)](#) models with α_{BC} and α_{ISM} to account for dust in the stellar birth clouds and the ISM.

The presence of an AGN can affect the resulting astrophysical quantities. PROSPECT has the ability to fit an AGN component using the [Fritz et al. \(2006\)](#) model, the UV-optical emission of which is also attenuated by the dust screen of the ISM. We denote the sets of SED fits with an AGN component included as Pro – Stellar + AGN while those with only stellar emission we call Pro – Stellar. Pro – Stellar has fewer parameters (see tab.2 in [Thorne et al. 2021](#)) than Pro – Stellar + AGN (see Tab. 1 in [Thorne et al. 2022a](#)) because there is no significant AGN component to be modelled. The optimal solution likely resides somewhere between these two that we refer to as Pro – Hybrid. Being guided by the principle of parsimony, Pro – Hybrid was obtained by first preferring Pro – Stellar for every SED fit and only swapping to Pro – Stellar + AGN when the likelihood of the Pro – Stellar + AGN was preferred and the AGN contribution to the rest-frame fitted SED at $5 - 20 \mu\text{m}$ was more than 10 per cent. This metric and threshold for significant AGN is the same as that outlined by [Dale et al. \(2014\)](#); [Thorne et al. \(2022a\)](#).

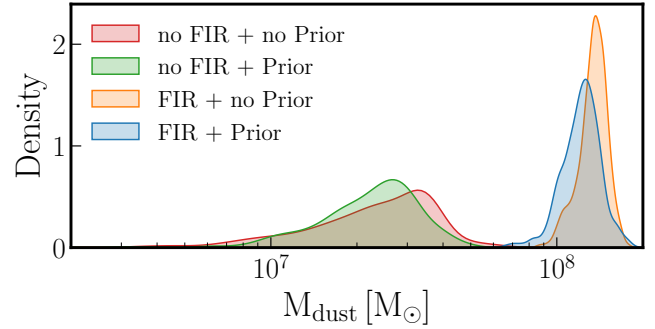


Figure 2. Posterior distributions of the dust mass from PROSPECT fits to the inverse-variance weighted stack of a sample of $z \approx 0.05$ galaxies with $S/N > 5$ FIR *Herschel* $P100, P160, S250, S350, S500$ photometric measurements. The blue curve shows the results when including the FIR measurements and a Gaussian prior on α with mean $\mu = 2$ and dispersion $\sigma = 1$. The orange curve shows the results including when including the FIR measurements but no prior. The green curve shows the results when excluding the FIR measurements and using the prior. The red curve shows the results when excluding both the FIR measurements and the prior.

3 CALCULATING THE DUST MASS

As we wish to derive the contribution of dust to the cosmic baryon inventory, it is important to discuss how the dust mass is inferred from SED fitting with PROSPECT.

In principle, the dust mass can be found by integrating Equation 2 over U once α has been fitted and the proportionality constant, which connects the strength of the radiation field to the dust emission, is known. Alternatively and more simply, the [Dale et al. \(2014\)](#) models calculate the IR-FIR emission for 1 M_\odot of dust and so the total dust mass of a galaxy is found by comparing the absorbed luminosity as per the [Charlot & Fall \(2000\)](#) model with the bolometric luminosity of the fitted [Dale et al. \(2014\)](#) model (more discussion on this is in Section 3.2). In terms of the dust mass, the salient parameters are $\tau_V^{\text{BC}}, \tau_V^{\text{ISM}}, \alpha_{\text{BC}}$ and α_{ISM} that together control the dust attenuation ([Charlot & Fall 2000](#)) and re-emission ([Dale et al. 2014](#)) for the two component dust model.

3.1 Dust masses without FIR photometry

The same dust that is attenuating the blue star light is re-radiating at redder wavelengths in the FIR. Hence, the dust mass is inferred from assumptions about the absorbed luminosity and the shape of the thermal emission spectrum and the dust temperature. DEVILS becomes more and more important at higher and higher redshifts. The fraction of sources with FIR measurements diminishes with redshift (as shown in Figure 1), which has implications for the constraints of dust temperature and, therefore, dust mass. To explore this, the inverse-variance weighted stacked SED of a sample of $z \approx 0.05$ GAMA galaxies with $S/N > 5$ photometry in all of the FIR *Herschel* $P100, P160, S250, S350, S500$ photometric bands was obtained and the SED was fit with and without FIR photometric measurements. The posterior distributions of the dust masses are shown in Figure 2.

It is clear that the absence of the FIR introduces significant uncertainty on the dust mass, as evident from the difference in the variance of the posterior distributions, because of the sensitivity on the dust temperature. The PROSPECT fits therefore used a Gaussian prior on each of the α parameters with dispersion $\sigma = 1$ and mean $\mu = 2$, which is the middle value of the range of $\alpha \in [0, 4]$ considered for

SED fitting (Thorne et al. 2021, 2022a). The inclusion of the FIR also systematically produces ≈ 0.7 dex more dust mass because the fit prefers $\alpha \approx 3$ and therefore cooler dust than for $\alpha = 2$. This is also why including this prior on α results in a less sharply peaked posterior distribution.

There is evidence that the dust temperature increases with redshift (e.g., Magnelli et al. 2014; Liang et al. 2019; Chiang et al. 2025), meaning that $\alpha \approx 3$ is unsurprising for this low redshift sample. The temperature from Wien's law and the peak of the fitted FIR emission was ≈ 25 K for $\alpha = 3$ and ≈ 68 K for $\alpha = 2$. This test shows, as a worst case scenario, that without FIR measurements the dust mass is highly sensitive to the assumption about the dust temperature. The Gaussian prior on α was set under the assumption that the dust is hotter at high redshift than low, especially in regard for the DEVILS galaxies. Fortunately, the situation at high redshift can be improved with joint observations from, for example, the *James Webb Space Telescope* and the *Atacama Large Millimeter Array* (e.g., Casey et al. 2024)

3.2 Dust mass modelling assumptions

Driver et al. (2018); Dunne et al. (2011); Pozzi et al. (2020); Beeston et al. (2024); Berta et al. (2025) all used the SED fitting code MAGPHYS (Da Cunha et al. 2008) to infer dust masses for the purpose of calculating the CDMH. MAGPHYS characterises the total IR-FIR emission as an ensemble of grey body radiators where the relative contributions and their temperatures are fitted parameters.

Both MAGPHYS and PROSPECT require robust measurements of the FIR emission, lest the dust masses be highly uncertain, as discussed in Section 3.1. To explore the intrinsic differences between the two SED fitting codes, we isolated a sample of 218 galaxies with $S/N > 5$ in the *Herschel* P100, P160, S250, S350, S500 photometric bands in both the PROFOUND catalogue (Bellstedt et al. 2020a) used for the PROSPECT SED fitting of this work and the LAMBDA catalogue (Wright et al. 2016) used for the MAGPHYS fitting in Driver et al. (2018).

Figure 3 shows the comparison between PROSPECT and MAGPHYS for this robust sample. The top panel shows an inverse-variance weighted stack of the SED of the robust sample, showing relative consistency between the two photometry tools. The bottom panel shows the histogram of the differences between the dust masses. Even with robust constraints on the FIR emission, PROSPECT infers ≈ 0.5 dex higher dust masses than MAGPHYS, meaning that the difference is mostly due to the different modelling assumption between codes and not from differences in the constraints of the FIR emission.

The MAGPHYS model includes contributions from birth clouds, inhabited by stars less than 10 Myr old, and the ISM. Each of those components contains a further contribution from ~ 100 K dust in the MIR, PAH emission using the template of Madden et al. (2006), warm dust of ≈ 50 K and cold dust of ≈ 20 K. These components are assumed to have fractional contributions to the total IR-FIR emission such that the total of each contribution must sum to 1. For further details on the dust model in MAGPHYS, the reader is directed to Da Cunha et al. (2008) and in particular Eqs. 13-22. The dust masses on the other hand are calculated only from the contributions of the warm component in the birth clouds and the warm and cold components in the ISM, assuming that they are grey body radiators (Hildebrand 1983). The contribution from the MIR and PAH emission is not explicitly accounted for because, as argued in Da Cunha et al. (2008), PAHs only contribute a few percent of the total dust mass (e.g., Draine et al. 2007; Sutter et al. 2024; Aniano et al. 2020), and

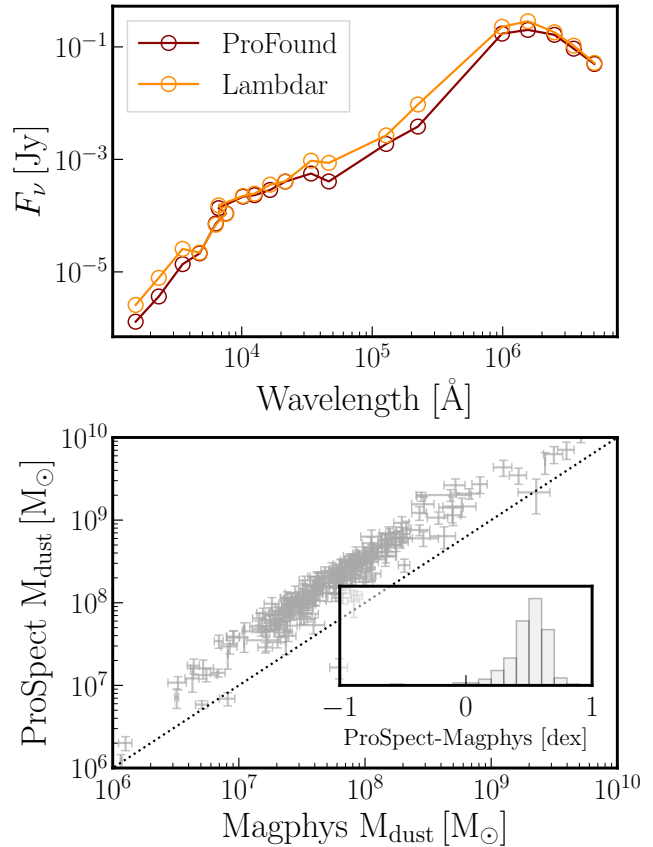


Figure 3. Top: inverse-variance weighted stacked SEDs of the 218 galaxies with $S/N > 5$ in the *Herschel* P100, P160, S250, S350, S500 photometric bands from both PROFOUND and LAMBDA photometry. Bottom: PROSPECT dust masses and 1σ uncertainties against MAGPHYS. The grey dotted line is the equality line. The inset panel is the histogram of the dust mass differences between PROSPECT and MAGPHYS

the final dust mass in MAGPHYS is therefore simply scaled up by 10 per cent.

The Dale et al. (2014) models provide the dust emission templates in units of $[\text{W}/\text{H}_{\text{atom}}]$. Therefore, in PROSPECT the luminosity for a $1 M_\odot$ of dust is calculated as

$$(M/L_i)^{-1} = \int_0^\infty \frac{f_i(\lambda)/\lambda}{L_\odot m_H/M_\odot \text{DTH}} d\lambda, \quad (3)$$

and the total dust mass of a galaxy fitted by a given Dale et al. (2014) template, $f_i(\lambda)$, is found by dividing its total absorbed luminosity from the Charlot & Fall (2000) model by $(M/L_i)^{-1}$. A key assumption in PROSPECT is a constant dust-to-hydrogen mass ratio (DTH) of $\text{DTH} = 0.0073$ that is the expected value for solar metallicity in the Milky Way (Draine et al. 2007). The assumption is that the DTH is assumed to be the same for all dust species that emit across the breadth of the electromagnetic spectrum meaning that the mass-to-light ratio for all dust species are the same.

However, PAH molecules that emit in predominantly the MIR are believed to only contribute a few per cent of the total mass in dust despite their significant contribution to the SED (Draine et al. 2007; Sutter et al. 2024; Aniano et al. 2020). The Dale et al. (2014) models were originally constructed from grain mixtures of very small grains, PAHs and big grains, before being combined into a total emission model. The big grains dominate the mass and the FIR emission,

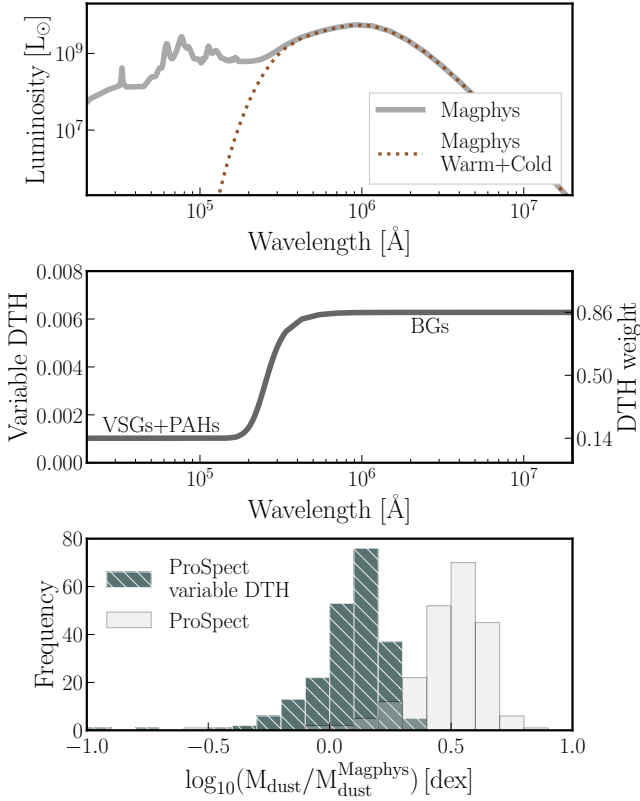


Figure 4. *Top:* MAGPHYS standard SED model. The thick grey line is for the total luminosity while the brown, dotted line is only the mass contributing part of the SED. *Middle:* variable DTH as a function of wavelength. The left axis denotes the DTH per wavelength while the right axis denotes the factor that DTH = 0.0073 is multiplied by. The regimes at which very small grains (VSGs), PAHs and big grains (BGs) dominate the emission are noted. *Bottom:* histogram comparison of dust masses between MAGPHYS. The light grey histogram is the same comparison in Figure 3. The dark histogram is the comparison against MAGPHYS using the updated dust masses and the variable DTH.

whereas the remaining dust species contribute less mass and mostly emit in the MIR (Dale & Helou 2002; Desert et al. 1990). Because of this we recalculated the PROSPECT dust masses by weighting the DTH as a function of wavelength to account for the difference in the mass contribution between grain species.

Figure 4 shows the calculation of our variable DTH, where we took the ratio of the standard MAGPHYS template of the mass contributing SED to the total SED as the weighting to apply to DTH = 0.0073. It can be seen that this variable DTH is close in form to a piecewise function,

$$DTH(\lambda) \propto \begin{cases} q & \lambda \leq 2 \times 10^5 \text{ \AA} \\ 1 - q & \lambda \geq 2 \times 10^5 \text{ \AA} \end{cases} \quad (4)$$

where q is the fraction of mass in PAHs+very small grains and the proportionality is the total DTH. Using $q = 0.14$ the refined dust masses with the updated variable DTH agree with the dust masses from MAGPHYS. This value of $q = 0.14$ is the same that was used for the grain mixture in the construction of the Desert et al. (1990); Dale & Helou (2002) models, on which the Dale et al. (2014) were based. The reader is reminded that the dust mass in MAGPHYS includes a 10 per cent scaling. On average, the dust masses are lowered by ≈ 2.5 times; hence, this is expected to be the origin of the higher

dust masses that we infer with PROSPECT. It must be stressed however that this scaling is sensitive to the value of q . For example, $q = 0.1$ results in ≈ 3.1 times lower dust masses.

In addition to a variable DTH per dust species, there is convincing evidence that the DTH changes with the gas-phase metallicity, with metal poorer systems having lower DTH (e.g., Casasola et al. 2020; Péroux & Howk 2020; Galliano et al. 2021; Park et al. 2024). The dust masses from GAMA and DEVILS were corrected for this effect by rescaling the DTH with the broken power law fit to the Z – DTH from Rémy-Ruyer et al. (2014, $X_{\text{CO},Z}$, see their Tab. 1) as a function of the Z_{final} fitted value from PROSPECT.

3.3 Additional dust mass caveats

We advocate that the main driver of the factor of ≈ 3 difference between the MAGPHYS dust masses and those directly from PROSPECT is the assumption of the fixed DTH = 0.0073. However, MAGPHYS and the models of Dale et al. (2014) also differ in their implementation of the emissivity index, β , for the greybody FIR emission, described as,

$$\text{greybody}_\lambda(\beta, T_{\text{dust}}) \propto \lambda^{-\beta} B_\lambda(T_{\text{dust}}), \quad (5)$$

where $B_\lambda(T_{\text{dust}})$ is the Planck function. MAGPHYS uses $\beta = 1.5$ for warm dust and $\beta = 2.0$ for cold dust. Dale et al. (2014) connect the emissivity index to the strength of the radiation field, U , that is heating the ensemble of dust masses (see Equation 2),

$$\beta = 2.5 + 0.4 \log_{10}(U). \quad (6)$$

The effect of this is similar to the implementation in MAGPHYS, with lower U values, and hence colder dust, corresponding to larger β values; and the range of assumed U values corresponds to $0.5 \lesssim \beta \lesssim 3$.

To better understand what effect this has on the dust mass between the two models, we fitted single-temperature greybody functions to the *Herschel* photometry of the sample of 218 FIR detected galaxies that were used to compare MAGPHYS and PROSPECT in Section 3.2. Figure 5 shows how different assumptions of β compared to a fixed value of $\beta = 2$ affect the dust mass. In no case of $0.5 \lesssim \beta \lesssim 3$ (the extrema of the Dale et al. (2014) models) is the average difference in the dust mass close to a factor of 3. We, therefore, expect that the difference in β between Dale et al. (2014) and MAGPHYS cannot be the main driver of the dust mass difference.

While we anticipate that the implementation of β is not significantly different enough between the models to affect the dust mass, the opacity coefficient normalised at $850\mu\text{m}$, $\kappa_{850\mu\text{m}}$, could be important. $\kappa_{850\mu\text{m}}$ is an essential parameter to obtain the absolute dust mass in MAGPHYS, and the assumption is that $\kappa_{850\mu\text{m}} = 0.077 \text{ kg m}^{-2}$ for all galaxies (Dunne et al. 2000). The dust mass from the single-temperature greybody scales with $\kappa_{850\mu\text{m}}$ such that the dust masses from MAGPHYS could have been ≈ 3 times higher had $\kappa_{850\mu\text{m}} = \frac{1}{3} 0.077 \text{ kg m}^{-2}$.

James et al. (2002) found that on average $\kappa_{850\mu\text{m}} = 0.07 \pm 0.02 \text{ kg m}^{-2}$. More recently, Clark et al. (2019) found that $\kappa_{500\mu\text{m}} = 0.11 - 0.25 \text{ kg m}^{-2}$ in M74 and $\kappa_{500\mu\text{m}} = 0.15 - 0.80 \text{ kg m}^{-2}$ in M83 using spatially resolved maps, demonstrating that $\kappa_{500\mu\text{m}}$ varies between these two galaxies and as a function of the local density of the ISM.

The opacity at $500\mu\text{m}$ can be connected to the opacity at $850\mu\text{m}$ as $\kappa_{850\mu\text{m}} = \kappa_{500\mu\text{m}} (500/850)^\beta$, where β is the emissivity index. From the ranges of $\kappa_{500\mu\text{m}}$ from those two galaxies and values of $\beta = 1.5 - 2$, it is clear that on average $\frac{1}{3} 0.077 < \kappa_{850\mu\text{m}} < 0.077 \text{ kg m}^{-2}$ for M74 and M83. So, despite Clark et al. (2019) finding lower $\kappa_{850\mu\text{m}}$ values

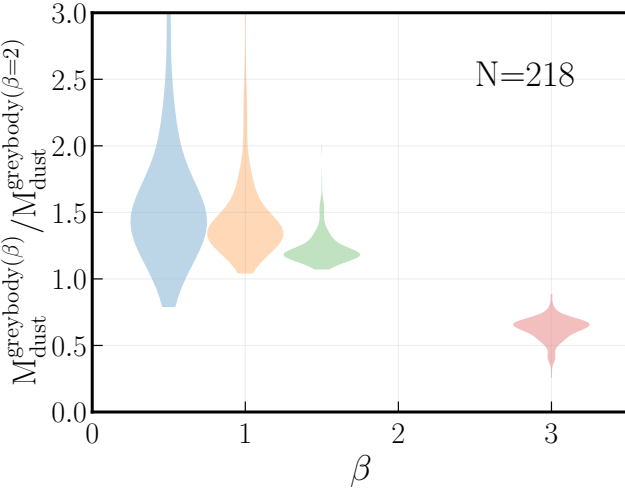


Figure 5. Comparison of the dust mass from fitting 218, FIR detected galaxies with single-temperature greybody functions. We show the distributions of the ratio of dust masses when varying the emissivity index, β , compared to a fixed value of $\beta = 2$, which is similar to the assumed implementation in MAGPHYS.

than $\kappa_{850\mu\text{m}} = 0.077 \text{ kg m}^{-2}$, it is still not enough to entirely explain the factor of ≈ 3 difference of dust mass between MAGPHYS and PROSPECT. This is true provided that M74 and M83 are representative of all the galaxies used in this work. Ultimately, we cannot rule out an uncertain $\kappa_{850\mu\text{m}}$ as causing differences in the dust masses between codes, but nevertheless maintain that a variable DTH is at least an improvement on what was originally assumed in PROSPECT.

4 FITTING THE SMF

While the contribution of dust to the baryon inventory is the focus of this work, we first calculated the stellar mass contribution. The stellar mass distribution function (SMF) is calculated as,

$$\phi(M_\star) = \frac{dN}{dM_\star dV}, \quad (7)$$

which is the histogram (dN) of stellar masses (dM_{star}) per unit comoving volume (dV). The volume depends on the survey area and the limits of the redshift bins. We split our sample of GAMA and DEVILS into bins spanning 0.75 Gyr of lookback time between 0 and 12 Gyr ago (corresponding to $z \approx 3.6$ in our cosmology), which was the same binning used by Thorne et al. (2021) for their calculations of the SMFs.

We made this calculation separately for GAMA and DEVILS as they cover different areas on the sky, with GAMA covering 217.54 deg² and DEVILS-D10 covering 1.5 deg². Both of these surveys are volume complete up to a certain magnitude, meaning that the stellar mass bin at which the distribution turns down may be adopted as the incompleteness limit as per the Malmquist Bias (e.g., Weigel et al. 2016). We identified the maximum of the binned SMF for each GAMA and DEVILS and set that as the mass limit. The SMFs for both GAMA and DEVILS were then combined for a single SMF, leveraging the superior depth of DEVILS for the less massive end and the superior spatial coverage of GAMA for the massive end. This was essentially the same strategy used by Driver et al. (2018) to compute the SMF by combining different surveys. Thorne et al.

(2021) had previously presented SMFs at $0 < z < 4$ using PROSPECT fits of DEVILS galaxies, and so the main improvement upon that work presented here is the inclusion of GAMA.

When the slope of the SMF is steep, the uncertainties on the stellar masses can systematically change the shape of the intrinsic SMF compared to what is observed (i.e., Eddington bias, Obreschkow et al. 2018). The uncertainties on the SED fitted stellar masses were propagated onto the SMF through a Monte-Carlo experiment by varying their values within their 1σ uncertainties and recomputing the binned SMF 1000 times, and this was combined in quadrature with the Poisson uncertainties of the SMF. A final error floor of 10 per cent on the SMF binned quantities was assumed to, at the very least, accommodate remaining systematic uncertainties.

With the sets of binned stellar mass distributions and corresponding uncertainties across the 16 bins of redshift at $0 < z \lesssim 3$, we fitted the SMF with double Schechter functions, which was the same function used in Thorne et al. (2021). The function is:

$$\phi(M_\star) = \ln(10) e^{-\mu} \left(\phi_1 \mu^{\alpha+1} + \phi_2 \mu^{\beta+1} \right), \quad (8)$$

where $\mu = 10^M/10^{M^*}$ and $M = \log_{10}(M_\star/M_\odot)$. The fitting software HIGHLANDER¹, which combines genetic optimisation and Markov-Chain-Monte-Carlo, was employed to find the maximum of the likelihood and the optimal solution of the parameters of the double Schechter functions. The top left panel of Figure 6 shows our fitted SMFs in each of the 16 redshift bins.

Because of large scale structure (LSS), the stellar mass distribution throughout 3D space is not necessarily expected to be uniform, which is reflected in the noisy redshift evolution of the fit parameters, particularly M^* and the two normalisation parameters. GAMA is overall underdense at $z < 0.1$ (Driver et al. 2022), which is also confirmed by the significantly lower M^* and ϕ_1 at the lowest redshift compared to the results at higher redshifts. The COSMOS field also contains a large number of galaxy clusters at $0.36 < z < 1$ (Finoguenov et al. 2007; Bellagamba et al. 2011).

To mitigate LSS, each of the five double Schechter function parameters were fit with quadratic polynomials in redshift, as shown by the filled lines in each of the bottom panels in Figure 6. This allowed us to compute a smooth, regressed SMF in each redshift bin, shown in the top right panel in Figure 6. This was the same kind of fit employed by Wright et al. (2018); Thorne et al. (2021) for their own calculations of the evolution of the SMF. The fit parameters of the double Schechter functions and the regressed fits are presented in Table A1 and Table A2.

4.1 LSS correction

Multiplying the x - and y -axes of the SMFs in Figure 6 results in the stellar mass density distributions and their integrals give the CSMH as a function of redshift, i.e.,

$$\rho_\star(z) = \int_0^\infty \phi(M_\star, z) \times M_\star dM_\star. \quad (9)$$

Figure 7 shows the CSMH. Signatures of LSS are evident in the noisy behaviour of the CSMH obtained from integrating the direct fits to the SMFs, particularly with our lowest redshift data point being ≈ 0.14 dex lower than the $z = 0$ measurement from Driver et al. (2022) in the GAMA fields.

The regressed CSMH, which comes from the quadratic fits to the double Schechter parameter evolution with redshift, show a smooth

¹ <https://github.com/asgr/HIGHLANDER>

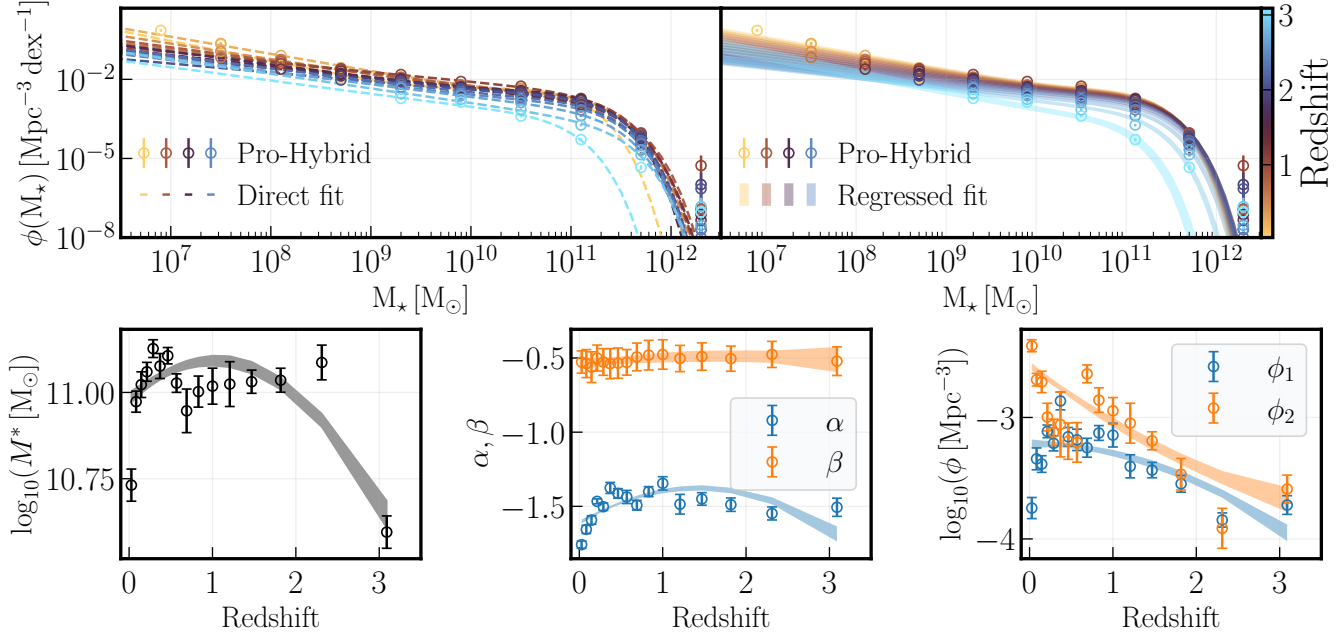


Figure 6. Top left: SMFs (points with 1σ uncertainties, in some bins the size of the error bar is smaller than the points) and double Schechter function fits (dashed lines) from $z \approx 0$ (yellow-red) to $z \approx 3$ (blue). Bottom: redshift evolution and 1σ uncertainties of $\log_{10}(M^*)$ (left), α, β (middle) and ϕ_1, ϕ_2 (right) as indicated in the legend. The shaded lines in all plots are the fits and 1σ uncertainties to the evolution which are quadratic in redshift. Top right: the regressed SMFs from the quadratic fits to the parameter evolution. The width of the lines is the 1σ spread on the regressed SMFs. The colour scheme is the same as the top left panel. The fit parameters are presented in Table A1 and Table A2.

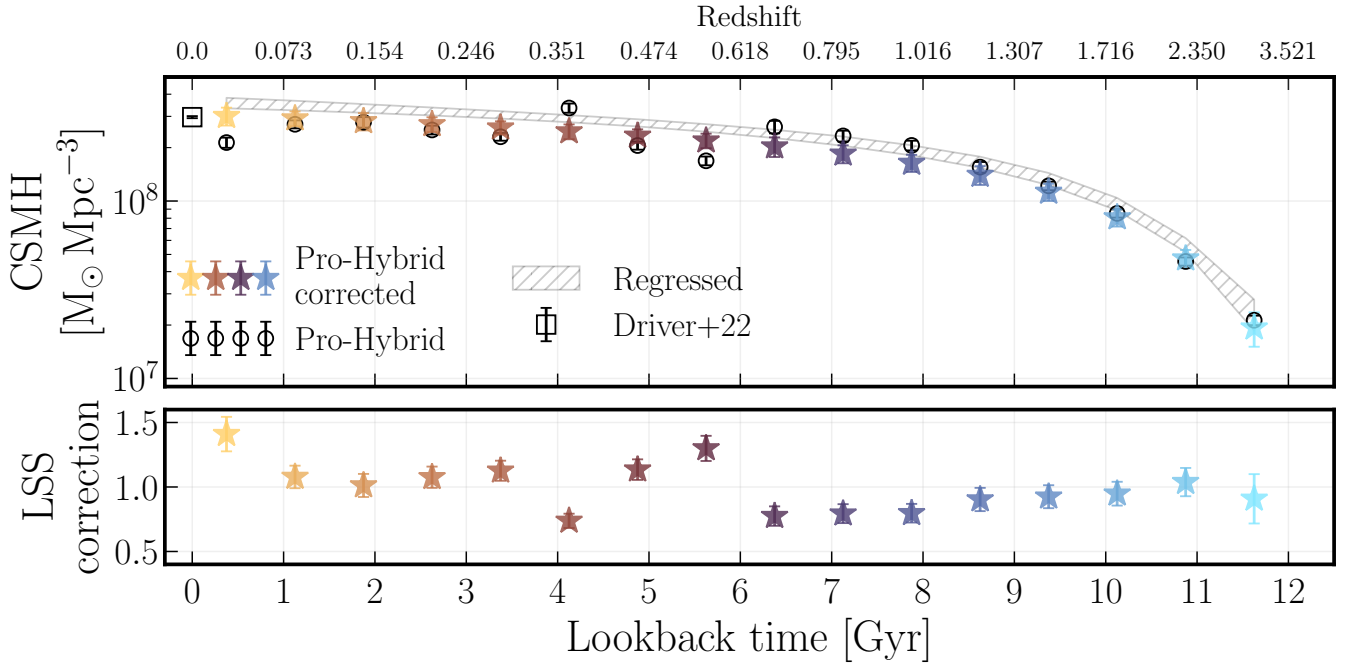


Figure 7. Top: the CSMH. The black circles with error bars are the values and 1σ uncertainties from the direct double Schechter function fits to the SMF). The hatched grey line is the CSMH and 1σ uncertainties from the regressed SMFs. The coloured stars and error bars are the values and 1σ uncertainties corrected for LSS. The square and error bars is the measurement and 1σ uncertainty at $z = 0$ from Driver et al. (2022). Bottom: the LSS correction factor and 1σ uncertainties, obtained by comparing the regressed CSMH to the direct CSMH.

evolution by construction. The level of bias induced on the CSMH from LSS was obtained by fitting the normalisation of the regressed, smooth evolution to the direct integrals of the SMFs. This allowed us to compute a global LSS correction factor, shown in the bottom panel of Figure 7, that is the factor by which the stellar mass density at each redshift must be multiplied to account for the presence of LSS. The corrected CSMH agrees well with [Driver et al. \(2022\)](#) at $z = 0$, validating this approach. The uncertainties on the LSS correction factors were propagated through to the uncertainties on the CSMH.

5 COSMIC DUST MASS HISTORY

Having accounted for the stars in the cosmic baryon inventory in Section 4, we now turn our attention to the dust. We computed the dust mass distribution functions (DMFs) using the same calculations as for the stars. Figure 8 shows the fitted DMFs for the Pro – Hybrid set in each of our 16 redshift bins. It can be seen that overall, the double Schechter functions adequately represent the data. Notably, the completeness limits that we derived from the maxima of the distributions of each GAMA and DEVILS indeed show that the method of combining these datasets in this way is valid. DEVILS dominates the contribution to the DMF at the low-mass/faint end at all redshifts and GAMA dominates the contribution at the massive end, similar to the SMFs. The DMF as a function of redshift shows very similar evolution as the stellar mass function, with a high-mass component becoming more prominent toward $z \approx 0$ (e.g., [Baldry et al. 2012](#); [Davidzon et al. 2017](#); [Grazian et al. 2015](#); [Leja et al. 2020](#); [Muzzin et al. 2013](#); [Thorne et al. 2021](#); [Weaver et al. 2023](#); [Wright et al. 2018](#)).

We compare our DMF to results from [Dunne et al. \(2011\)](#); [Pozzi et al. \(2020\)](#); [Beeston et al. \(2024\)](#); [Berta et al. \(2025\)](#) who all used SED fitting techniques to infer the dust masses. The fit parameters of the double Schechter functions presented in Table A3. There is overall agreement between our work and those from the literature.

It should be noted that the correction factor applied to the dust masses for the variable DTH in detail depends on the α parameter in the [Dale et al. \(2014\)](#) dust models, but we have opted instead to shift the dust masses lower by an average factor of ≈ 2.5 , assuming that the distribution of α parameters marginalises out when computing the binned DMF (and furthermore when integrating the DMF for the CDMH). Indeed, it can be seen from the comparison of dust masses in Figure 3 that the difference is basically constant over the range of dust masses.

Figure 9 shows the CDMH computed from the fitted DMFs. Some tension is noticeable at $0.35 \lesssim z \lesssim 0.6$ where our results are ≈ 0.15 dex lower than, for example, [Driver et al. \(2018\)](#). However, this may be due to cosmic variance because, as can be seen from the LSS correction factors in Figure 7, there is some indication that the COSMOS region is under-dense compared to the cosmic mean in that redshift range ([Bellagamba et al. 2011](#)) and could have skewed their results to lower values.

Our results show a similar decline of the CDMH past its peak as [Driver et al. \(2018\)](#), which is expected since the dust masses are inferred with similar methods of FUV-FIR SED fitting. The decline from the results of [Dunne et al. \(2011\)](#); [Pozzi et al. \(2020\)](#); [Beeston et al. \(2024\)](#); [Eales & Ward \(2024\)](#); [Chiang et al. \(2025\)](#) is similar to ours up until $z \approx 0.4$, at which point the slope of our CDMH is ≈ 0.5 times less steep compared to the average of those results (i.e., we inferred a shallower decline of the CDMH over the last ≈ 4 Gyr). At $z > 1$ our results agree with those from the literature ([Eales & Ward 2024](#); [Berta et al. 2025](#); [Chiang et al. 2025](#)), within the uncertainties.

It is worth discussing the metallicity-dependent DTH correction, as described in Section 3.2. The effect of this correction on the CDMH is negligible below $z \approx 1.3$ as the Universe is on average enriched to solar metallicity. When the DTH for solar metallicity was used, the CDMH at $z \gtrsim 1.3$ was $\approx 0.1 - 0.3$ dex higher than the CDMH calculated with the metallicity-dependent DTH and shown in Figure 9. This meant that the metallicity-dependent correction was important to better resolve the peak of the CDMH, as opposed to a plateau at $z \gtrsim 1.3$.

5.1 CDMH Comparison to simulations

The corrected CDMH generally follows a similar evolution to the cosmic star formation history with a peak around $z \approx 1 - 2$. It can be seen that the slope of the CDMH below $z \approx 0.5$ is shallower than the slope of the cosmic star formation history ([D'Silva et al. 2023, 2025](#)). Dust is formed from metals that are themselves produced during stellar evolution (e.g., [Draine 2003](#); [Ginolfi et al. 2018](#)) through the mechanisms of stellar winds off AGB stars ([Ventura et al. 2014](#); [Höfner & Olofsson 2018](#); [Höfner & Freytag 2020](#)) and supernovae explosions ([Nomoto et al. 2006](#); [Bocchio et al. 2016](#); [Marassi et al. 2019](#); [Sarangi et al. 2018](#); [Schneider & Maiolino 2024](#)), and so the expectation is that the CDMH is controlled by the cosmic star formation history. At the same time, dust grains in the ISM may be destroyed in the ISM and consumed via star formation ([Draine & Salpeter 1979b,a](#); [Jones et al. 1994, 1996](#); [Micelotta et al. 2018](#)). The CDMH is hence a useful quantity to compare against simulations as it depends intricately on the sub-grid implementations of feedback and star formation.

Indeed, the consensus from simulations is that the decline of the CDMH closely follows the cosmic star formation history, though with a delay in response to the balance between dust growth and destruction as the star formation decreases ([Popping et al. 2017](#); [Vijayan et al. 2019](#); [Triani et al. 2020](#); [Parente et al. 2023](#)). In Figure 10 we compare our CDMH with semi-analytic models: L-GALAXIES ([Parente et al. 2023](#)) and SHARK ([Lagos et al. 2024](#)), and hydrodynamic models: SIMBA ([Davé et al. 2019](#); [Li et al. 2019](#)) and COLIBRE ([Schaye et al. 2025](#); [Trayford et al. 2025](#)).

In general, our fully corrected CDMH is mostly in agreement with these simulations at $z \lesssim 0.4$. We remark that SHARK and COLIBRE predict a shallower decline below $z \approx 0.4$ than both L-GALAXIES and SIMBA. The difference between these two sets of simulations at $z \lesssim 0.4$ are more than likely due to their implementation of stellar feedback that both suppresses the star formation/chemical enrichment and destroys the dust/expels it from the galaxy. We estimate ≈ 0.1 dex higher values of the CDMH at $z > 0.4$ compared to all simulations.

6 THE BARYON INVENTORY

In addition to the DTH, [Rémy-Ruyer et al. \(2014\)](#) also report the dust-to-gas mass ratio (DTG) that is essentially the DTH plus the mass in helium and metals. The metallicity dependent DTG was used to convert the GAMA and DEVILS dust masses to total neutral gas masses, using the Z_{final} parameter from PROSPECT. With the neutral gas masses we computed the neutral gas mass distribution functions (GMFs) that were fitted with double Schechter functions. The results are shown in Figure 11 and the fit parameters are presented in Table A4.

Integrating the GMFs we computed the cosmic neutral gas mass history (CGMH), shown as the green band in Figure 12. We note that this includes the factor of ≈ 2.5 down-scaling as used for the CDMH.

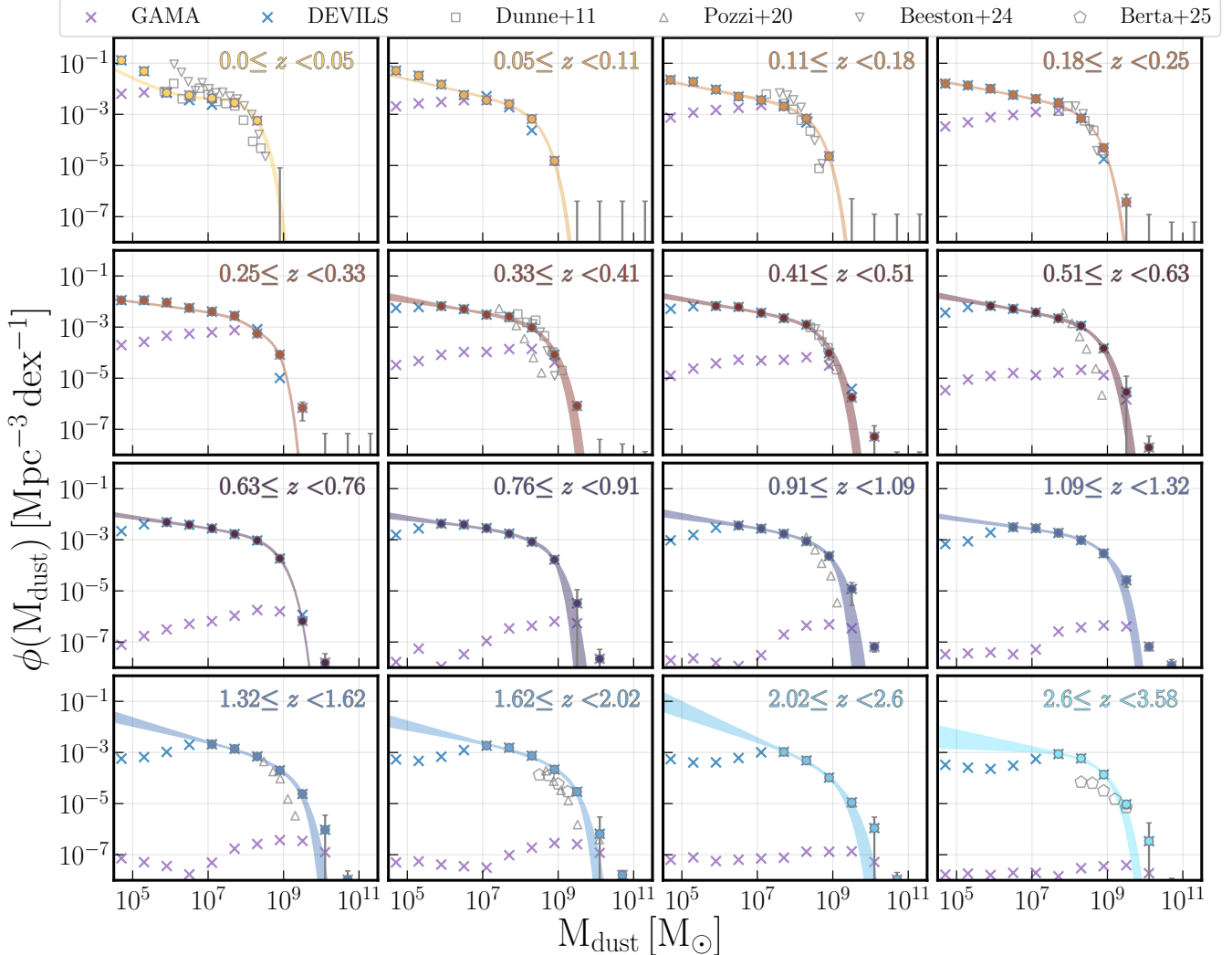


Figure 8. The DMF at $0 < z \lesssim 3$ as indicated in the legend. In every panel, the solid points with 1σ error bars are the combined binned quantities from GAMA and DEVILS. The filled curves show the double Schechter functions and the 1σ uncertainty range. The fit parameters are presented in Table A3. The binned quantities for GAMA and DEVILS are shown independently with purple and blue crosses. We show results from Dunne et al. (2011); Pozzi et al. (2020); Beeston et al. (2024); Berta et al. (2025) with grey symbols as indicated in the legend.

The shape of the CGMH inferred from the dust mass shows remarkable agreement with previous results from the compilations presented in Walter et al. (2020). It is however clear that the normalisation of our CGMH underestimates the HI mass density, especially at $z < 1$ where the measurements are from 21 cm observations (though there is scatter between the results from the compilation of Walter et al. 2020). The average difference over all redshift is ≈ 0.6 dex lower.

We expect that our lower CGMH is due to differences in the spatial distributions of dust, from which our neutral gas masses are inferred, and HI in galaxies. Our dust masses are confined within the optical radius as per the source detection, photometric extraction and SED fitting. In contrast, the mass of HI within the optical radius can be between 20 – 100 per cent of the total HI mass (e.g., Lee et al. 2025). Moreover, our lowest redshift point for the neutral gas density is ≈ 0.3 dex lower than Dev et al. (2024), potentially because Dev et al. (2024) calculated the gas content in the dark matter haloes, covering a larger spatial extent of neutral gas than traced by dust. The CGMH tends to more closely agree with the H_2 gas mass density from the

compilation in Walter et al. (2020), where, unlike the HI, the molecular gas and dust are expected to have similar spatial distributions in galaxies. We note that the DTG ratio that we used was calculated within the aperture of the dust emission (Rémy-Ruyer et al. 2014) and so does not account for neutral gas beyond the optical radius.

The contribution to the baryon inventory from SMBHs was inferred from the cosmic AGN luminosity history as presented in D'Silva et al. (2023, 2025) who used the same GAMA and DEVILS data also used here to compute this quantity at $0 < z < 3$. The cosmic SMBH history was inferred by assuming a 10 per cent radiative efficiency and successively integrating down to $z = 0$ (e.g., Shakura & Sunyaev 1973).

In Figure 12, we compare all of our baryon measurements to a swath of results from the literature of the cosmic stellar mass densities (Driver et al. 2018; Wright et al. 2018; Thorne et al. 2021; Driver et al. 2022; Shuntov et al. 2025), neutral gas mass densities (Walter et al. 2020; Dev et al. 2024), SMBH mass densities (Graham et al. 2007; Vika et al. 2009; Shen et al. 2020) and, as previously

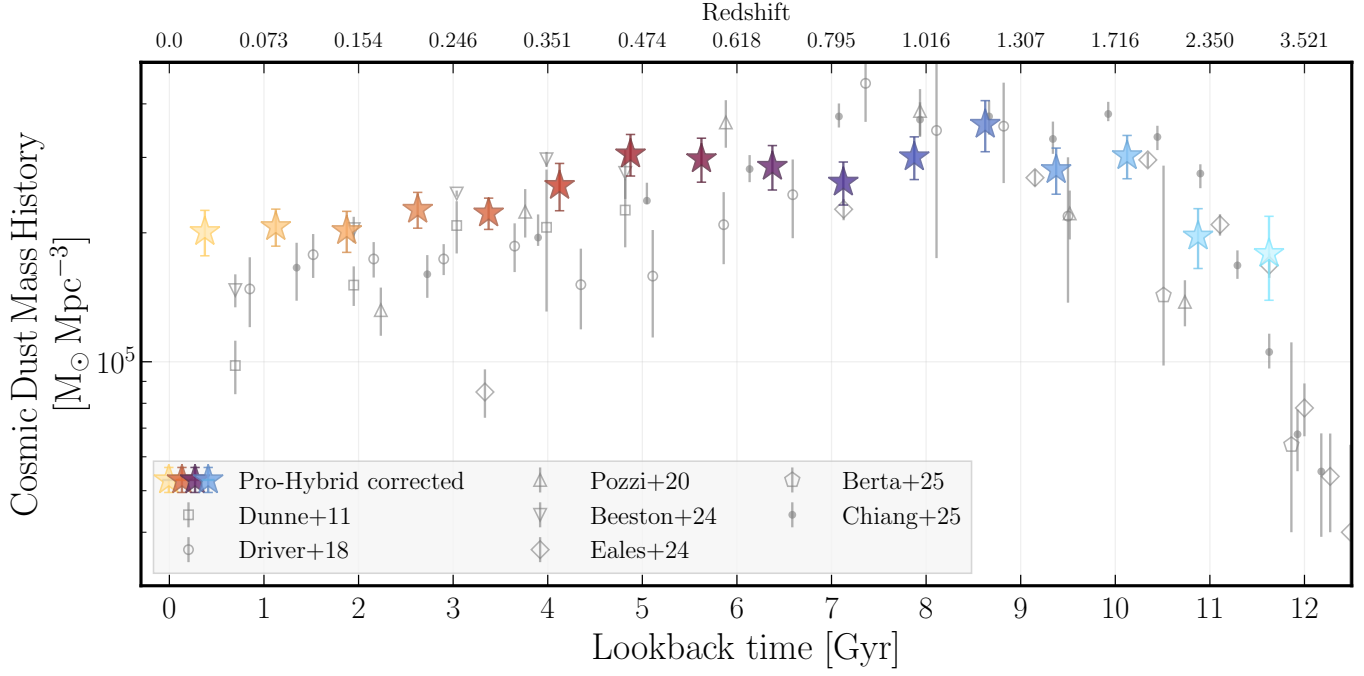


Figure 9. The CDMH. The coloured stars with error bars are the values and 1σ uncertainties using the Pro – Hybrid SED fits. This CDMH was both scaled down by a factor of ≈ 2.5 and corrected for the metallicity dependent DTH as per the discussion in Section 3.2. This has been corrected for LSS using the factors in Figure 7. We show previous measurements and 1σ uncertainties as indicated (Dunne et al. 2011; Driver et al. 2018; Pozzi et al. 2020; Beeston et al. 2024; Eales & Ward 2024; Chiang et al. 2025; Berta et al. 2025).

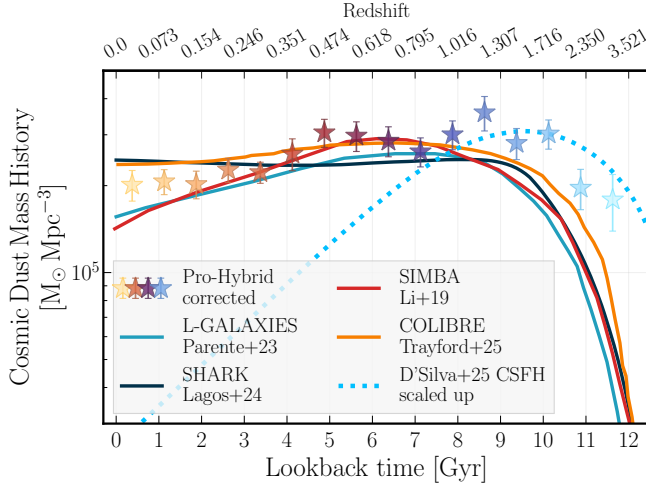


Figure 10. Comparison of the CDMH with simulations. The colourful points and error bars are the same as in Figure 9. We show simulation predictions (Li et al. 2019; Parente et al. 2023; Lagos et al. 2024; Trayford et al. 2025) as indicated in the figure legend. The dotted blue line is the cosmic star formation history from D'Silva et al. (2023, 2025) scaled up by $\approx 4 \times 10^6$.

discussed, dust mass densities (Dunne et al. 2011; Driver et al. 2018; Pozzi et al. 2020; Beeston et al. 2024; Eales & Ward 2024; Chiang et al. 2025; Berta et al. 2025). We find overall agreement between our baryon census and previous results from the literature. The novelty of our work is demonstrated in Figure 12 because every quantity of the mass density was calculated using essentially the same data (GAMA and DEVILS) and methods (i.e., PROSPECT) throughout, meaning

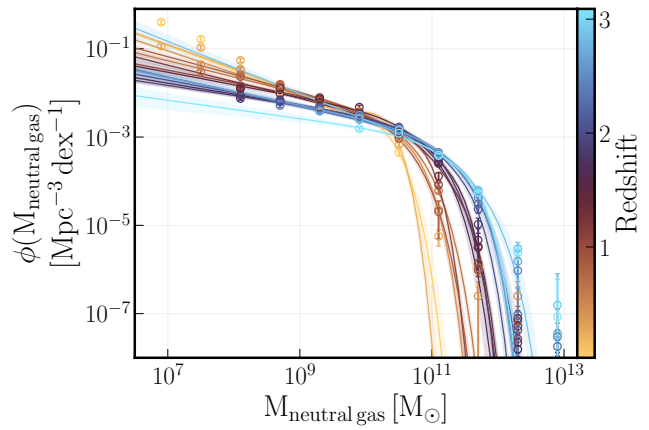


Figure 11. The dust-traced GMFs at $0 < z \lesssim 3$, as indicated in the legend, for Pro – Hybrid. The filled curves show the double Schechter functions and the 1σ uncertainty range. The fit parameters are presented in Table A4.

that this census of the baryons is self-consistent. The results for the stars, dust and neutral gas are presented in Table A5.

The baryon inventory of today is quantified in relation to the cosmic baryon density, which as predicted by Λ CDM is $\Omega_b \approx 0.05$ (Aghanim et al. 2020), in units of the critical density, $\rho_{\text{crit},0} = \frac{3H_0^2}{8\pi G}$. We find that stars, neutral gas, SMBHs and dust within the optical radii of galaxies account for ≈ 5 per cent of the baryon budget. This value has grown from ≈ 1 per cent over the last ≈ 12 Gyr up to the present. Notably, we have not accounted for hot gas in the interstellar, circumgalactic or intergalactic medium (e.g. Ferrière 2001; Draine

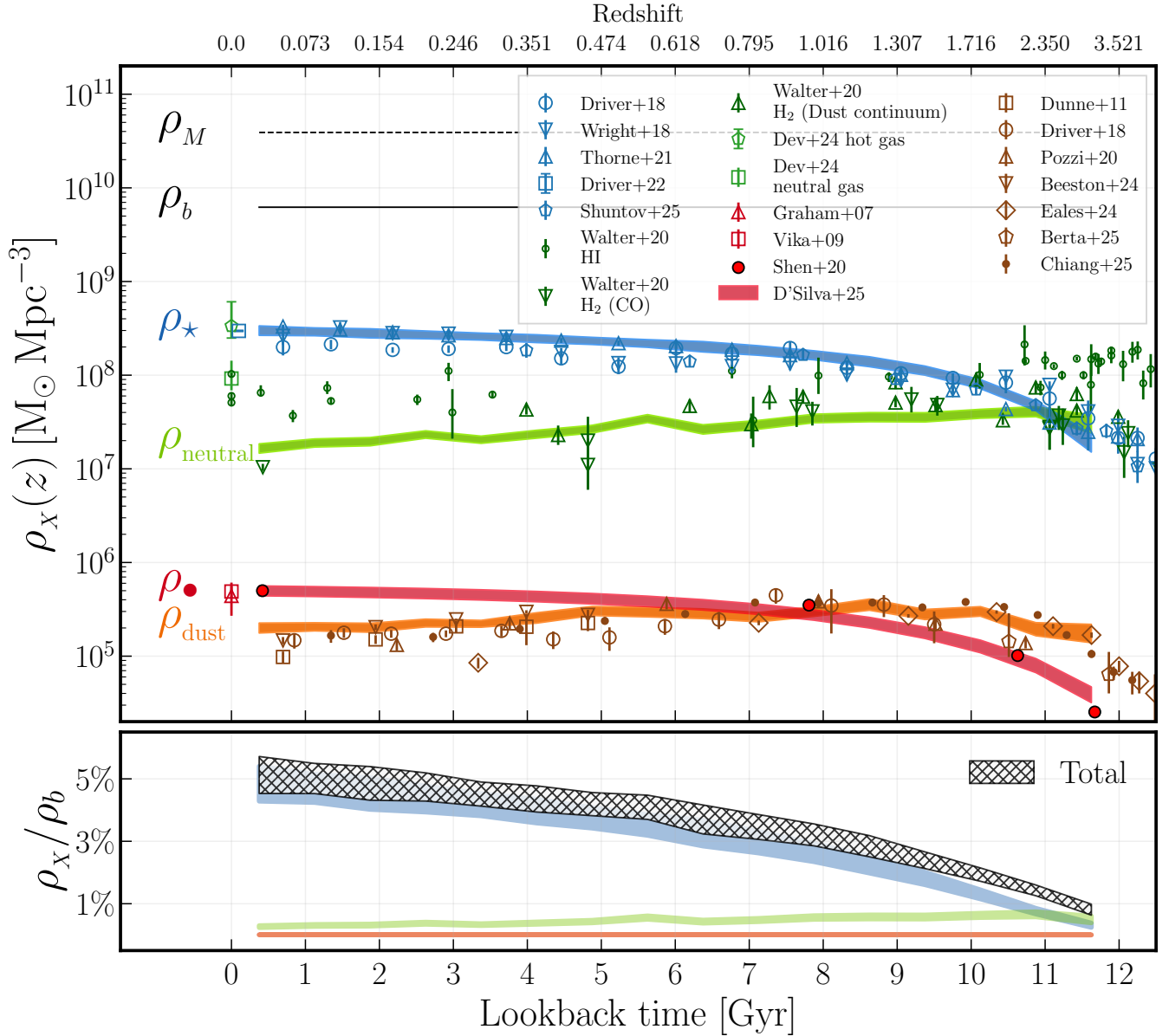


Figure 12. *Top:* cosmic mass densities and the baryon inventory. The blue curve shows the CSMH from the regressed fits of the SMFs. The orange filled curve shows the results of the CDMH. The green filled curve is the CGMH. All of these have had the LSS correction applied. The red curve shows the supermassive black hole mass history from D’Silva et al. (2023, 2025), which is inferred from the AGN luminosity history by assuming a 10 per cent radiative efficiency and successively integrating down to $z = 0$. The solid line is the baryon density and the dashed line is the total matter density from Λ CDM. Observations and 1σ uncertainties of the stellar mass densities (Driver et al. 2018; Wright et al. 2018; Thorne et al. 2021; Driver et al. 2022; Shuntov et al. 2025), gas mass densities (Walter et al. 2020; Dev et al. 2024), SMBH mass densities (Graham et al. 2007; Vika et al. 2009; Shen et al. 2020) and the same literature results of the dust mass densities from Figure 9 are shown in blue, green, red and brown as indicated in the figure legend. *Bottom:* baryon fraction obtained by dividing the curves in the top panel with the baryon density. The total baryon fraction in galaxies is shown as the grey filled region. The colour scheme is the same as the top panel. The results for the stars, dust and neutral gas are presented in Table A5.

2011; Tumlinson et al. 2017). The measurement of the hot, X-ray emitting gas density from Dev et al. (2024) is at the same level as the stellar mass at $z = 0$. Hence, many of the remaining baryons are expected to be spread throughout the dark matter haloes of galaxies and the cosmic web (e.g., Fukugita & Peebles 2004; de Graaff et al. 2019) in the form of ionised gas (Macquart et al. 2020; Wright et al. 2024; Connor et al. 2025).

7 CONCLUSIONS

In this paper, we have investigated the volume-averaged evolution of stars, neutral gas, SMBHs and dust in galaxies over the last ≈ 12 Gyr using GAMA and DEVILS. The main results are summarised below:

- (i) We computed the stellar, dust and neutral gas mass distribution functions in 16 redshift bins, uniformly spaced in 0.75 Gyr intervals

of lookback time. Each of these were fitted with double Schechter functions.

(ii) Integrating those we obtained the cosmic stellar, dust and neutral gas mass history at $0 < z < 3$. The cosmic dust mass history in particular follows a similar shape to the cosmic star formation history, peaking at $z \approx 1 - 2$ and declining thereafter up to the present. The decline is interpreted as a balance between the slowing down of dust production and destruction, both due to the decrease of star formation down to $z = 0$.

(iii) Using the dust masses directly from PROSPECT resulted in ≈ 3 times higher dust masses than previous results with the SED fitting code MAGPHYS. In fact, this difference will persist between any code that also employs modified blackbody dust emission. We expect that the main reason behind this is due to the assumption of a uniform mass-to-light ratio assumed for all IR-FIR emitting dust species in PROSPECT. If we instead assumed that PAH molecules and very small grains, which emit predominantly at $\lambda \lesssim 2 \times 10^5 \text{ \AA}$, contribute no more than $\approx 10 - 14$ per cent of the total dust mass, the resulting dust masses came into better agreement with MAGPHYS.

(iv) We compared the CDMH with both the semi-analytic models, SHARK and L-GALAXIES, and the hydrodynamic models, SIMBA and COLIBRE. We found that all of the simulations are mostly in agreement with the CDMH at $z \lesssim 0.4$. SHARK and COLIBRE exhibit a shallower decline at $z < 0.4$ compared to SIMBA and L-GALAXIES pointing to differences in the implementation of dust growth and destruction between the two sets of models. We estimated ≈ 0.1 dex higher values of the CDMH at $z > 0.4$ compared to all simulations.

(v) Dividing the dust masses by the metallicity dependent dust-to-gas ratio of Rémy-Ruyer et al. (2014), we obtained neutral gas masses from which we calculated the neutral gas mass distribution functions and the cosmic neutral gas mass density, finding broad agreement with previous results. The gas mass density traced by the dust is ≈ 0.6 dex lower than that inferred from 21cm observations, more than likely because of the different spatial extents covered by dust and HI in galaxies.

(vi) Folding in previous measurements of the cosmic SMBH mass densities that were also computed on the same data sets of GAMA/DEVILS and in an identical manner, we presented a self-consistent and homogeneous census of the baryon inventory in galaxies. Stars, neutral gas, SMBHs and dust within the optical radii of galaxies constitute about 5 per cent of the baryon budget. This means that most of the remaining 95 per cent of baryons must be diffuse ionised gas residing in the interstellar, circumgalactic and intergalactic medium.

ACKNOWLEDGEMENTS

JCJD is supported by the Australian Government Research Training Program (RTP) Scholarship. CL is a recipient of the ARC Discovery Project DP210101945. AJB. and EdC. acknowledge support from the Australian Research Council (project DP240100589).

DEVILS is an Australian project based around a spectroscopic campaign using the Anglo-Australian Telescope. DEVILS is part funded via Discovery Programs by the Australian Research Council and the participating institutions. The DEVILS website is devils.research.org.au.

DATA AVAILABILITY

The analysis scripts and data can be found on GitHub here: <https://github.com/JordanDSilva/dust-mass-density>. Data from the GAMA survey may be found here: <https://www.gama-survey.org>. The DEVILS data are hosted and provided by AAO Data Central (datacentral.org.au).

REFERENCES

Aghanim N., et al., 2020, *Astronomy & Astrophysics*, 641, A6
 Aniano G., et al., 2020, *The Astrophysical Journal*, 889, 150
 Baldry I. K., et al., 2012, *Monthly Notices of the Royal Astronomical Society*, 421, 621
 Beeston R. A., Gomez H. L., Dunne L., Maddox S., Eales S. A., Smith M. W. L., 2024, *Monthly Notices of the Royal Astronomical Society*, 535, 3162
 Bellagamba F., Maturi M., Hamana T., Meneghetti M., Miyazaki S., Moscardini L., 2011, *Monthly Notices of the Royal Astronomical Society*, 413, 1145
 Bellstedt S., et al., 2020a, *Monthly Notices of the Royal Astronomical Society*, 496, 3235
 Bellstedt S., et al., 2020b, *Monthly Notices of the Royal Astronomical Society*, 498, 5581
 Berta S., et al., 2025, *Astronomy and Astrophysics*, 696, A193
 Bocchio M., Marassi S., Schneider R., Bianchi S., Limongi M., Chieffi A., 2016, *Astronomy & Astrophysics*, 587, A157
 Bosman S. E. I., et al., 2022, *Monthly Notices of the Royal Astronomical Society*, 514, 55
 Bruzual G., Charlot S., 2003, *Monthly Notices of the Royal Astronomical Society*, 344, 1000
 Casasola V., et al., 2020, *Astronomy and Astrophysics*, 633, A100
 Casey C. M., Akins H. B., Kokorev V., McKinney J., Cooper O. R., Long A. S., Franco M., Manning S. M., 2024, *The Astrophysical Journal Letters*, 975, L4
 Chabrier G., 2003, *Publications of the Astronomical Society of the Pacific*, 115, 763
 Charlot S., Fall S. M., 2000, *The Astrophysical Journal*, 539, 718
 Chiang Y.-K., Makiya R., Ménard B., 2025, *eprint arXiv:2504.05384*, p. arXiv:2504.05384
 Clark C. J. R., et al., 2019, *Monthly Notices of the Royal Astronomical Society*, 489, 5256
 Connor L., et al., 2025, *Nature Astronomy*
 D'Silva J. C. J., et al., 2023, *Monthly Notices of the Royal Astronomical Society*, 524, 1448
 D'Silva J. C. J., et al., 2025, *arXiv e-prints*, p. arXiv:2503.03431
 Da Cunha E., Charlot S., Elbaz D., 2008, *Monthly Notices of the Royal Astronomical Society*, 388, 1595
 Dale D. A., Helou G., 2002, *The Astrophysical Journal*, 576, 159
 Dale D. A., Helou G., Contursi A., Silbermann N. A., Kohatkar S., 2001, *The Astrophysical Journal*, 549, 215
 Dale D. A., Helou G., Magdis G. E., Armus L., Díaz-Santos T., Shi Y., 2014, *The Astrophysical Journal*, 784, 83
 Davé R., Anglés-Alcázar D., Narayanan D., Li Q., Rafieferantsoa M. H., Appleby S., 2019, *Monthly Notices of the Royal Astronomical Society*, 486, 2827
 Davidzon I., et al., 2017, *Astronomy & Astrophysics*, 605, A70
 Davies L. J. M., et al., 2016, *Monthly Notices of the Royal Astronomical Society*, 461, 458
 Davies L. J. M., et al., 2018, *Monthly Notices of the Royal Astronomical Society*, Volume 480, Issue 1, p. 768-799, 480, 768
 Davies L. J. M., et al., 2021, *Monthly Notices of the Royal Astronomical Society*, 506, 256
 Davies L. J. M., et al., 2025, *Monthly Notices of the Royal Astronomical Society*, Volume 544, Issue 4, pp. 3005-3040, 36 pp., 544, 3005
 Dayal P., et al., 2022, *Monthly Notices of the Royal Astronomical Society*, 512, 989

Desert F.-X., Boulanger F., Puget J. L., 1990, *Astronomy and Astrophysics*, 237, 215

Dev A., Driver S. P., Meyer M., Robotham A., Obreschkow D., Popesso P., Comparat J., 2024, *Monthly Notices of the Royal Astronomical Society*, 535, 2357

Draine B. T., 2003, *Annual Review of Astronomy and Astrophysics*, 41, 241

Draine B. T., 2011, *Physics of the Interstellar and Intergalactic Medium* by Bruce T. Draine. Published by Princeton University Press

Draine B. T., Salpeter E. E., 1979a, *The Astrophysical Journal*, 231, 77

Draine B. T., Salpeter E. E., 1979b, *The Astrophysical Journal*, 231, 438

Draine B. T., et al., 2007, *The Astrophysical Journal*, 663, 866

Driver S. P., et al., 2011, *Monthly Notices of the Royal Astronomical Society*, Volume 413, Issue 2, pp. 971-995., 413, 971

Driver S. P., et al., 2016, *The Astrophysical Journal*, Volume 827, Issue 2, article id. 108, \$<\\$NUMPAGES\$>\$15\$<\\$NUMPAGES\$>\$ pp. (2016)., 827, 108

Driver S. P., et al., 2018, *Monthly Notices of the Royal Astronomical Society*, 475, 2891

Driver S. P., et al., 2022, *Monthly Notices of the Royal Astronomical Society*, 513, 439

Dunne L., Eales S., Edmunds M., Ivison R., Alexander P., Clements D. L., 2000, *Monthly Notices of the Royal Astronomical Society*, Volume 315, Issue 1, pp. 115-139., 315, 115

Dunne L., et al., 2011, *Monthly Notices of the Royal Astronomical Society*, 417, 1510

Dunne L., Maddox S. J., Papadopoulos P. P., Ivison R. J., Gomez H. L., 2022, *Monthly Notices of the Royal Astronomical Society*, 517, 962

Eales S., Ward B., 2024, *Monthly Notices of the Royal Astronomical Society*, 529, 1130

Ferrière K. M., 2001, *Reviews of Modern Physics*, 73, 1031

Finoguenov A., et al., 2007, *The Astrophysical Journal Supplement Series*, 172, 182

Fritz J., Franceschini A., Hatziminaoglou E., 2006, *Monthly Notices of the Royal Astronomical Society*, 366, 767

Fukugita M., Peebles P. J. E., 2004, *The Astrophysical Journal*, 616, 643

Galliano F., et al., 2021, *Astronomy & Astrophysics*, 649, A18

Ginolfi M., Graziani L., Schneider R., Marassi S., Valiante R., Dell'Agli F., Ventura P., Hunt L. K., 2018, *Monthly Notices of the Royal Astronomical Society*, 473, 4538

Graham A. W., Driver S. P., Allen P. D., Liske J., 2007, *Monthly Notices of the Royal Astronomical Society*, 378, 198

Grazian A., et al., 2015, *Astronomy & Astrophysics*, 575, A96

Hildebrand R. H., 1983, *Quarterly Journal of the Royal Astronomical Society*, 24, 267

Höfner S., Freytag B., 2020, *Proceedings of the International Astronomical Union*, 16, 165

Höfner S., Olofsson H., 2018, *The Astronomy and Astrophysics Review*, 26, 1

James A., Dunne L., Eales S., Edmunds M. G., 2002, *Monthly Notices of the Royal Astronomical Society*, 335, 753

Jones A. P., Tielens A. G. G. M., Hollenbach D. J., McKee C. F., 1994, *The Astrophysical Journal*, 433, 797

Jones A. P., Tielens A. G. G. M., Hollenbach D. J., 1996, *The Astrophysical Journal*, 469, 740

Kennicutt Jr R. C., Evans II N. J., 2012, *Annual Review of Astronomy and Astrophysics*, 50, 531

Koushan S., et al., 2021, *Monthly Notices of the Royal Astronomical Society*, 503, 2033

Lagos C. d. P., et al., 2024, *Monthly Notices of the Royal Astronomical Society*, 531, 3551

Lee S., et al., 2025, *Publications of the Astronomical Society of Australia*, 42, e046

Leja J., Speagle J. S., Johnson B. D., Conroy C., van Dokkum P., Franx M., 2020, *The Astrophysical Journal*, 893, 111

Li Q., Narayanan D., Davé R., 2019, *Monthly Notices of the Royal Astronomical Society*, Volume 490, Issue 1, p.1425-1436, 490, 1425

Liang L., et al., 2019, *Monthly Notices of the Royal Astronomical Society*, 489, 1397

Lilly S. J., et al., 2009, *The Astrophysical Journal Supplement Series*, 184, 218

Lutz D., et al., 2011, *Astronomy & Astrophysics*, 532, A90

Macquart J.-P., et al., 2020, *Nature*, 581, 391

Madau P., Dickinson M., 2014, *Annual Review of Astronomy and Astrophysics*, 52, 415

Madden S. C., Galliano F., Jones A. P., Sauvage M., 2006, *Astronomy and Astrophysics*, 446, 877

Madden S. C., et al., 2020, *Astronomy & Astrophysics*, 643, A141

Magnelli B., et al., 2014, *Astronomy & Astrophysics*, 561, A86

Marassi S., Schneider R., Limongi M., Chieffi A., Graziani L., Bianchi S., 2019, *Monthly Notices of the Royal Astronomical Society*, 484, 2587

Matsuura M., et al., 2011, *Science*, 333, 1258

Micelotta E. R., Matsuura M., Sarangi A., 2018, *Space Science Reviews*, 214, 53

Muzzin A., et al., 2013, *The Astrophysical Journal*, 777, 18

Nomoto K., Tominaga N., Umeda H., Kobayashi C., Maeda K., 2006, *Nuclear Physics A*, 777, 424

Obreschkow D., Murray S. G., Robotham A. S. G., Westmeier T., 2018, *Monthly Notices of the Royal Astronomical Society*, 474, 5500

Oliver S. J., et al., 2012, *Monthly Notices of the Royal Astronomical Society*, 424, 1614

Parente M., Ragone-Figueroa C., Granato G. L., Lapi A., 2023, *Monthly Notices of the Royal Astronomical Society*, 521, 6105

Park H.-J., et al., 2024, *Monthly Notices of the Royal Astronomical Society*, 535, 729

Péroux C., Howk J. C., 2020, *Annual Review of Astronomy and Astrophysics*, 58, 363

Popping G., Somerville R. S., Galametz M., 2017, *Monthly Notices of the Royal Astronomical Society*, 471, 3152

Pozzi F., Calura F., Zamorani G., Delvecchio I., Gruppioni C., Santini P., 2020, *Monthly Notices of the Royal Astronomical Society*, 491, 5073

Rémy-Ruyer A., et al., 2014, *Astronomy and Astrophysics*, 563, A31

Robotham A. S. G., Davies L. J. M., Driver S. P., Koushan S., Tarau D. S., Casura S., Liske J., 2018, *Monthly Notices of the Royal Astronomical Society*, Volume 476, Issue 3, p.3137-3159, 476, 3137

Robotham A. S. G., Bellstedt S., Lagos C. d. P., Thorne J. E., Davies L. J., Driver S. P., Bravo M., 2020, *Monthly Notices of the Royal Astronomical Society*, 495, 905

Sanders D. B., et al., 2007, *The Astrophysical Journal Supplement Series*, 172, 86

Sarangi A., Matsuura M., Micelotta E. R., 2018, *Space Sci. Rev.*, 214, 63

Schaye J., et al., 2025, *arXiv e-prints*, p. arXiv:2508.21126

Schneider R., Maiolino R., 2024, *The Astronomy and Astrophysics Review*, 32, 2

Shakura N. I., Sunyaev R. A., 1973, *Astronomy and Astrophysics*, 24, 337

Shen X., Hopkins P. F., Faucher-Giguère C.-A., Alexander D. M., Richards G. T., Ross N. P., Hickox R. C., 2020, *Monthly Notices of the Royal Astronomical Society*, 495, 3252

Shuntov M., et al., 2025, *Astronomy & Astrophysics*, 695, A20

Somerville R. S., Davé R., 2015, *Annual Review of Astronomy and Astrophysics*, 53, 51

Sutter J., et al., 2024, *The Astrophysical Journal*, 971, 178

Thorne J. E., et al., 2021, *Monthly Notices of the Royal Astronomical Society*, 505, 540

Thorne J. E., et al., 2022a, *Monthly Notices of the Royal Astronomical Society*, 509, 4940

Thorne J. E., et al., 2022b, *Monthly Notices of the Royal Astronomical Society*, 517, 6035

Tompkins S. A., Driver S. P., Robotham A. S. G., Windhorst R. A., Lagos C. d. P., Vernstrom T., Hopkins A. M., 2023, *Monthly Notices of the Royal Astronomical Society*, 521, 332

Trayford J. W., et al., 2025, Modelling the Evolution and Influence of Dust in Cosmological Simulations That Include the Cold Phase of the Interstellar Medium, doi:10.48550/ARXIV.2505.13056

Triani D. P., Sinha M., Croton D. J., Pacifici C., Dwek E., 2020, *Monthly Notices of the Royal Astronomical Society*, 493, 2490

Trumpler R. J., 1930, *Publications of the Astronomical Society of the Pacific*,

Vol. 42, No. 248, p.214, 42, 214

Tumlinson J., Peebles M. S., Werk J. K., 2017, *Annual Review of Astronomy and Astrophysics*, 55, 389

Ventura P., Dell'Agli F., Schneider R., Di Criscienzo M., Rossi C., La Franca F., Gallerani S., Valiante R., 2014, *Monthly Notices of the Royal Astronomical Society*, 439, 977

Vijayan A. P., Clay S. J., Thomas P. A., Yates R. M., Wilkins S. M., Henriques B. M., 2019, *Monthly Notices of the Royal Astronomical Society*, 489, 4072

Vika M., Driver S. P., Graham A. W., Liske J., 2009, *Monthly Notices of the Royal Astronomical Society*, 400, 1451

Wakelam V., et al., 2017, *Molecular Astrophysics*, 9, 1

Walter F., et al., 2020, *The Astrophysical Journal*, 902, 111

Weaver J. R., et al., 2023, *Astronomy & Astrophysics*, 677, A184

Weigel A. K., Schawinski K., Bruderer C., 2016, *Monthly Notices of the Royal Astronomical Society*, 459, 2150

Wooden D. H., Rank D. M., Bregman J. D., Witteborn F. C., Tielens A. G. G. M., Cohen M., Pinto P. A., Axelrod T. S., 1993, *Astrophysical Journal Supplement v.88*, p.477, 88, 477

Wright A. H., et al., 2016, *Monthly Notices of the Royal Astronomical Society*, 460, 765

Wright A. H., Driver S. P., Robotham A. S. G., 2018, *Monthly Notices of the Royal Astronomical Society*, 480, 3491

Wright R. J., Somerville R. S., Lagos C. d. P., Schaller M., Davé R., Anglés-Alcázar D., Genel S., 2024, *Monthly Notices of the Royal Astronomical Society*, 532, 3417

Zanella A., et al., 2018, *Monthly Notices of the Royal Astronomical Society*, 481, 1976

de Graaff A., Cai Y.-C., Heymans C., Peacock J. A., 2019, *Astronomy & Astrophysics*, 624, A48

APPENDIX A: FIT PARAMETERS OF DISTRIBUTION FUNCTIONS

This paper has been typeset from a $\text{\TeX}/\text{\LaTeX}$ file prepared by the author.

$\langle z \rangle$	$\log_{10}(M^* [\text{M}_\odot])$	α	β	$\log_{10}(\phi_1 [\text{Mpc}^{-3}])$	$\log_{10}(\phi_2 [\text{Mpc}^{-3}])$
0.027	10.731 ± 0.047	-1.758 ± 0.024	-0.527 ± 0.075	-3.746 ± 0.087	-2.410 ± 0.049
0.084	10.973 ± 0.031	-1.655 ± 0.028	-0.537 ± 0.094	-3.341 ± 0.090	-2.689 ± 0.052
0.146	11.023 ± 0.037	-1.593 ± 0.029	-0.562 ± 0.103	-3.384 ± 0.068	-2.708 ± 0.088
0.214	11.060 ± 0.027	-1.466 ± 0.017	-0.500 ± 0.088	-3.114 ± 0.052	-2.997 ± 0.114
0.288	11.127 ± 0.026	-1.503 ± 0.025	-0.527 ± 0.090	-3.213 ± 0.062	-3.123 ± 0.109
0.371	11.077 ± 0.036	-1.376 ± 0.037	-0.538 ± 0.101	-2.864 ± 0.073	-3.058 ± 0.267
0.464	11.106 ± 0.024	-1.413 ± 0.032	-0.534 ± 0.102	-3.159 ± 0.076	-3.195 ± 0.150
0.569	11.027 ± 0.027	-1.437 ± 0.044	-0.529 ± 0.086	-3.184 ± 0.088	-3.206 ± 0.163
0.690	10.947 ± 0.063	-1.492 ± 0.033	-0.493 ± 0.093	-3.249 ± 0.078	-2.641 ± 0.074
0.832	11.002 ± 0.045	-1.401 ± 0.034	-0.481 ± 0.100	-3.128 ± 0.061	-2.857 ± 0.101
1.001	11.018 ± 0.052	-1.345 ± 0.045	-0.476 ± 0.099	-3.146 ± 0.098	-2.945 ± 0.109
1.208	11.024 ± 0.065	-1.486 ± 0.066	-0.503 ± 0.089	-3.402 ± 0.095	-3.047 ± 0.164
1.470	11.031 ± 0.034	-1.450 ± 0.042	-0.490 ± 0.092	-3.433 ± 0.063	-3.192 ± 0.074
1.818	11.035 ± 0.035	-1.489 ± 0.045	-0.504 ± 0.085	-3.546 ± 0.069	-3.468 ± 0.130
2.311	11.087 ± 0.050	-1.548 ± 0.044	-0.476 ± 0.088	-3.844 ± 0.058	-3.912 ± 0.165
3.090	10.595 ± 0.047	-1.506 ± 0.061	-0.521 ± 0.096	-3.721 ± 0.077	-3.589 ± 0.115

Table A1. Double Schechter function fit parameters and 1σ uncertainties for the SMFs. These fitted functions should be multiplied by the LSS correction factor to get the same CSMH as in Figure 7 and Table A5.

	C_0	C_1	C_2
$\log_{10}(M^* [\text{M}_\odot])$	10.981 ± 0.017	0.215 ± 0.038	-0.105 ± 0.014
α	-1.612 ± 0.013	0.330 ± 0.037	-0.115 ± 0.014
β	-0.540 ± 0.044	0.059 ± 0.086	-0.017 ± 0.030
$\log_{10}(\phi_1 [\text{Mpc}^{-3}])$	-3.215 ± 0.035	-0.002 ± 0.071	-0.077 ± 0.025
$\log_{10}(\phi_2 [\text{Mpc}^{-3}])$	-2.569 ± 0.034	-0.522 ± 0.082	0.053 ± 0.031

Table A2. Regressed fits and 1σ uncertainties to each of the double Schechter function parameters for the SMFs. Fits are quadratic in redshift, $C_0 + zC_1 + z^2C_2$.

$\langle z \rangle$	$\log_{10}(M^* [\text{M}_\odot])$	α	β	$\log_{10}(\phi_1 [\text{Mpc}^{-3}])$	$\log_{10}(\phi_2 [\text{Mpc}^{-3}])$
0.027	8.290 ± 0.050	-1.719 ± 0.034	-0.805 ± 0.068	-4.197 ± 0.147	-2.740 ± 0.050
0.084	8.626 ± 0.072	-1.331 ± 0.015	0.071 ± 0.710	-3.083 ± 0.050	-5.338 ± 1.851
0.146	8.672 ± 0.051	-1.277 ± 0.051	-0.651 ± 0.801	-3.086 ± 0.203	-4.071 ± 1.752
0.214	8.759 ± 0.024	-1.278 ± 0.012	0.418 ± 0.996	-3.142 ± 0.042	-5.296 ± 1.452
0.288	8.553 ± 0.023	-1.192 ± 0.012	1.500 ± 0.047	-3.024 ± 0.033	-4.000 ± 0.075
0.371	8.839 ± 0.113	-1.212 ± 0.052	0.594 ± 1.078	-2.957 ± 0.141	-5.108 ± 1.314
0.464	8.942 ± 0.096	-1.251 ± 0.038	0.885 ± 1.009	-3.194 ± 0.110	-5.671 ± 1.370
0.569	8.966 ± 0.102	-1.253 ± 0.047	0.328 ± 0.961	-3.303 ± 0.121	-5.455 ± 1.460
0.690	9.002 ± 0.043	-1.217 ± 0.028	0.103 ± 0.621	-3.141 ± 0.054	-4.466 ± 1.319
0.832	8.782 ± 0.254	-1.202 ± 0.055	0.997 ± 0.692	-3.084 ± 0.159	-3.804 ± 1.390
1.001	9.069 ± 0.253	-1.245 ± 0.050	0.767 ± 0.764	-3.202 ± 0.132	-4.539 ± 1.679
1.208	9.141 ± 0.085	-1.193 ± 0.032	0.809 ± 0.925	-3.228 ± 0.068	-5.399 ± 1.733
1.470	9.376 ± 0.210	-1.383 ± 0.073	0.660 ± 0.846	-3.683 ± 0.193	-4.602 ± 1.275
1.818	9.323 ± 0.219	-1.340 ± 0.075	0.982 ± 0.665	-3.599 ± 0.196	-4.708 ± 1.118
2.311	9.433 ± 0.171	-1.586 ± 0.109	0.338 ± 0.963	-4.080 ± 0.243	-6.240 ± 1.013
3.090	9.159 ± 0.109	-1.222 ± 0.135	0.275 ± 1.028	-3.562 ± 0.137	-6.117 ± 1.336

Table A3. Double Schechter function fit parameters and 1σ uncertainties for the DMFs. These fitted functions should be multiplied by the LSS correction factor and should be divided by ≈ 2.5 to get the same CDMH as in Figure 12 and Table A5.

$\langle z \rangle$	$\log_{10}(M^* [\text{M}_\odot])$	α	β	$\log_{10}(\phi_1 [\text{Mpc}^{-3}])$	$\log_{10}(\phi_2 [\text{Mpc}^{-3}])$
0.027	9.984 ± 0.113	-1.558 ± 0.020	-0.365 ± 0.298	-3.089 ± 0.069	-2.802 ± 0.190
0.084	9.724 ± 0.058	-1.523 ± 0.022	1.219 ± 0.377	-2.727 ± 0.070	-2.674 ± 0.093
0.146	10.304 ± 0.067	-1.497 ± 0.020	-0.183 ± 0.448	-3.057 ± 0.073	-3.029 ± 0.098
0.214	10.546 ± 0.046	-1.370 ± 0.014	0.378 ± 1.021	-2.978 ± 0.044	-4.583 ± 1.248
0.288	10.459 ± 0.063	-1.398 ± 0.031	0.153 ± 0.880	-2.980 ± 0.077	-6.171 ± 1.549
0.371	10.248 ± 0.024	-1.286 ± 0.028	1.465 ± 0.114	-2.636 ± 0.041	-3.283 ± 0.106
0.464	10.797 ± 0.033	-1.378 ± 0.029	1.500 ± 0.065	-3.218 ± 0.057	-4.733 ± 0.198
0.569	10.723 ± 0.019	-1.279 ± 0.022	1.500 ± 0.073	-3.051 ± 0.038	-4.299 ± 0.138
0.690	10.798 ± 0.102	-1.248 ± 0.029	0.128 ± 0.870	-2.981 ± 0.075	-4.118 ± 1.703
0.832	10.851 ± 0.044	-1.229 ± 0.017	0.125 ± 1.076	-2.969 ± 0.048	-4.904 ± 1.108
1.001	10.958 ± 0.052	-1.275 ± 0.022	1.313 ± 0.332	-3.066 ± 0.042	-4.312 ± 0.371
1.208	11.221 ± 0.055	-1.340 ± 0.023	1.094 ± 1.258	-3.374 ± 0.066	-5.134 ± 0.595
1.470	11.132 ± 0.102	-1.322 ± 0.068	0.614 ± 0.839	-3.306 ± 0.143	-4.451 ± 0.592
1.818	11.031 ± 0.077	-1.308 ± 0.038	1.267 ± 0.335	-3.232 ± 0.068	-4.115 ± 0.262
2.311	11.488 ± 0.089	-1.591 ± 0.050	0.252 ± 1.084	-3.850 ± 0.087	-5.254 ± 1.250
3.090	11.082 ± 0.064	-1.205 ± 0.056	1.063 ± 0.371	-3.325 ± 0.069	-4.122 ± 0.209

Table A4. Double Schechter function fit parameters and 1σ uncertainties for the GMFs. These fitted functions should be multiplied by the LSS correction factor and should be divided by ≈ 2.5 to get the same CGMH as in Figure 12 and Table A5.

$\langle z \rangle$	$\log_{10}(\rho_\star [\text{M}_\odot \text{Mpc}^{-3}])$	$\log_{10}(\rho_{\text{dust}} [\text{M}_\odot \text{Mpc}^{-3}])$	$\log_{10}(\rho_{\text{neutral}} [\text{M}_\odot \text{Mpc}^{-3}])$	LSS correction factor [dex]
0.027	8.479 ± 0.050	5.304 ± 0.053	7.220 ± 0.050	0.149 ± 0.041
0.084	8.465 ± 0.042	5.315 ± 0.043	7.278 ± 0.043	0.033 ± 0.035
0.146	8.449 ± 0.049	5.306 ± 0.048	7.292 ± 0.044	0.005 ± 0.038
0.214	8.432 ± 0.042	5.356 ± 0.042	7.368 ± 0.040	0.032 ± 0.033
0.288	8.414 ± 0.037	5.347 ± 0.036	7.313 ± 0.039	0.052 ± 0.030
0.371	8.392 ± 0.042	5.411 ± 0.055	7.372 ± 0.042	-0.132 ± 0.033
0.464	8.368 ± 0.038	5.485 ± 0.048	7.425 ± 0.041	0.055 ± 0.030
0.569	8.340 ± 0.041	5.474 ± 0.051	7.539 ± 0.042	0.114 ± 0.033
0.690	8.307 ± 0.055	5.456 ± 0.052	7.424 ± 0.049	-0.111 ± 0.042
0.832	8.266 ± 0.051	5.419 ± 0.050	7.473 ± 0.047	-0.101 ± 0.040
1.001	8.215 ± 0.048	5.478 ± 0.050	7.540 ± 0.046	-0.099 ± 0.039
1.208	8.147 ± 0.053	5.554 ± 0.059	7.554 ± 0.048	-0.044 ± 0.043
1.470	8.052 ± 0.048	5.448 ± 0.054	7.553 ± 0.049	-0.034 ± 0.042
1.818	7.907 ± 0.048	5.481 ± 0.050	7.590 ± 0.047	-0.023 ± 0.042
2.311	7.676 ± 0.051	5.293 ± 0.069	7.614 ± 0.053	0.016 ± 0.046
3.090	7.286 ± 0.095	5.253 ± 0.096	7.489 ± 0.094	-0.042 ± 0.091

Table A5. Measurements and 1σ uncertainties for the CSMH, CDMH and CGMH as in Figure 12. Each of these columns and the uncertainties factor in the LSS corrections and their associated uncertainties, which are themselves presented in the rightmost column. The CDMH and CGMH include corrections for the metallicity-dependent DTH and have been lowered by ≈ 2.5 as per the discussion in Section 3.2.